Check for updates

Analysis of influencing factors on wellbore instability for high-pressure gas well during testing and production

Hailong Jiang[1,2], Mian Chen[1]*, Chao Hua[3], Xiao Li[2] and Yong Zhang[2]

[1]State Key Laboratory of Petroleum Resources and Prospecting, China University of Petroleum, Beijing, China, [2]College of Mechanical Engineering, Xi'an Shiyou University, Xi'an, Shannxi, China, [3]Xi'an Qing'an Electrical Control Co., Ltd, Xi'an, Shannxi, China

Unlike normal-pressure gas wells, wellbore instability is more likely to occur during testing for high-pressure gas wells. Gas acceleration effect exists in gas flow during high-pressure gas well testing, which was ignored in previous wellbore instability analysis. In this paper, the developments of effective circumferential stress and effective radial stress are analyzed in the near-wellbore area of high-pressure gas well, considering the influence of *in-situ* stress non-uniformity and acceleration effect. To analyze the effective circumferential stress and the effective radial stress more accurately, it is established that the fluid-structure coupling stress field of the finite large thick wall cylinder The flow field considers three cases, namely Darcy's law, Darcy−Forchheimer model and Darcy-Forchheime model considering gas acceleration. The results show that *in-situ* stress non-uniformity has a similar influence on tensile failure and shear failure. It is observed that the location of occurring shear failure and tensile failure may not be on the wellbore wall. When the formation fluid is under abnormally high pressure, it is more likely to have a tensile failure, while when the formation fluid is under abnormally low pressure, it is more likely to have a shear failure. The Biot parameter has the same effect on tensile failure and shear failure. These results are helpful to control sand production during testing and production for high-pressure gas wells.

KEYWORDS
acceleration effect, non-uniform *in situ* stress, wellbore instability, tensile failure, shear failure

1 Introduction

High-pressure gas reservoirs are characterized by natural fractures, high formation pressure and large variation of a production pressure difference which is on account of depletion production. In the process of gas test production, the non-Darcy characteristic of high speed is the prominent characteristic of high-pressure gas flow, which is not only manifested in the inertial resistance, but also in the significant gas acceleration effect induced by the rapid expansion of the gas volume (Jin et al., 2011a; Chen et al., 2011; Jin et al., 2012). The characteristic makes the spatio-temporal evolution of gas pressure more complex (Jin et al., 2019; Zhang et al., 2021; Hou et al., 2022a; Zhang et al., 2022). Traditionally, the inertial effect of near-wellbore gas flow is simply expressed by adding the Forchheimer inertial drag to Darcy's Law. However, this description of the inertial effects of compressible fluid flows is incomplete. Wooding (1957) might be the first to add an accelerated-inertial term to the gas momentum equation. The model with the accelerated-inertial term has been discussed in detail for a high-speed compressible flow in porous media (Nield, 1994; Levy et al., 1995; Chang and Hou, 2022). Jiang et al. (2015a; 2015b; 2015c; 2016) finds the reason why the gas

acceleration effect was ignored in the past literature and analyzes the importance of the gas acceleration effect in detail. Jin et al. (2011b) establishes a plane radial model considering the acceleration effect and presents a method for quantitative evaluation of the gas acceleration effect. Tensile stress is easy to form in the surrounding rock stress of the wellbore wall considering the acceleration effect by analyzing the fluid-structure coupling stress equation in the infinite thick-walled cylinder. The relationship of effective radial stress under different seepage models is not pointed out. Wellbore instability failure is usually divided into two categories, one is a shear failure, and the other is a tension failure. The current research focuses on shear failure (Zhao et al., 2021; Hou et al., 2022b; Hou et al., 2022c; Warsitzka et al., 2022), while the strength of extension is frequently used in analyzing tensile failure for wellbore instability during testing and production (Tan et al., 2021; Hou et al., 2022d; Sun et al., 2022; Hou et al., 2022e; Huang et al., 2023).

In this paper, we investigate the properties of near-wellbore stress using a set of equations that is built in the finite thick-walled cylinder in the non-uniform *in-situ* stress field. It is proved that the acceleration effect increases the possibility of tensile and shear failure. It is shown that the two types of failure do not necessarily occur on the wellbore wall. It is also shown that when the formation fluid is under abnormally high pressure, it is more likely to have a tensile failure, while when the formation fluid is under abnormally low pressure, it is more likely to have a shear failure. The Biot parameter has the same effect on tensile failure and shear failure.

2 Wellbore stress distributions in the finite large thick wall cylinder model

The stratum is assumed to be a uniform isotropic, linear elastic porous material, and the surrounding rock is considered to be in a plane strain state. σ_H is the horizontal maximum stress and σ_h is the horizontal minimum stress. The stress distributions for a radially varying pore pressure given by Eqs. (4.51)–(4.52) in the literature (Fjaer et al., 2008) is under the uniform stress field. The wellbore stress under the non-uniform *in-situ* stress can be obtained by changing both equations according to the theory of elasticity. The new wellbore stress distributions are:

$$
\begin{aligned}
\sigma_r &= \frac{(\sigma_H + \sigma_h)}{2}\left(\frac{R_e^2}{R_e^2 - R_w^2} - \frac{R_e^2 R_w^2}{(R_e^2 - R_w^2)r^2}\right) + \frac{R_w^2(R_e^2 - r^2)p_w}{r^2(R_e^2 - R_w^2)} \\
&+ \frac{(\sigma_H - \sigma_h)}{2}\left(\frac{R_e^2(R_e^4 + R_e^2 R_w^2 + 4R_w^4)}{(R_e^2 - R_w^2)^3} + \frac{3R_e^4 R_w^4(R_e^2 + R_w^2)}{(R_e^2 - R_w^2)^3 r^4}\right. \\
&\left. - 4\frac{R_e^2 R_w^2(R_e^4 + R_e^2 R_w^2 + R_w^4)}{(R_e^2 - R_w^2)^3 r^2}\right)\cos 2\theta \\
&+ \frac{2\eta}{r^2}\left[\int_{R_w}^{r} r'\Delta p(r')dr' - \frac{r^2 - R_w^2}{R_e^2 - R_w^2}\int_{R_w}^{R_e} r'\Delta p(r')dr'\right] \\
\sigma_\theta &= \frac{(\sigma_H + \sigma_h)}{2}\left(\frac{R_e^2}{R_e^2 - R_w^2} + \frac{R_e^2 R_w^2}{(R_e^2 - R_w^2)r^2}\right) - \frac{R_w^2(R_e^2 + r^2)p_w}{r^2(R_e^2 - R_w^2)} \\
&- \frac{(\sigma_H - \sigma_h)}{2}\left(\frac{R_e^2(R_e^4 + R_e^2 R_w^2 + 4R_w^4)}{(R_e^2 - R_w^2)^3} + \frac{3R_e^4 R_w^4(R_e^2 + R_w^2)}{(R_e^2 - R_w^2)^3 r^4}\right. \\
&\left. - \frac{12R_e^2 R_w^2 r^2}{(R_e^2 - R_w^2)^3}\right)\cos 2\theta + 2\eta\Delta p(r) \\
&- \frac{2\eta}{r^2}\left[\int_{R_w}^{r} r'\Delta p(r')dr' + \frac{r^2 + R_w^2}{R_e^2 - R_w^2}\int_{R_w}^{R_e} r'\Delta p(r')dr'\right]
\end{aligned}
\tag{1}
$$

where $\eta = (1 - 2v_{fr})\alpha_B/2(1 - v_{fr})$ is the poroelastic coefficient, $\Delta p(r) = p(r) - p_e$, and v_{fr} is the rock frame Poisson ratio.

When σ_H is equal to σ_h, Equation 1 will be simplified to Eqs. (4.51)–(4.52) in the literature (Fjaer et al., 2008). The dimensionless stress distributions related to Equation 1 are:

$$
\begin{aligned}
\sigma_r &= \frac{A}{2}\left(\frac{R_e^2}{R_e^2 - 1} - \frac{R_e^2}{(R_e^2 - 1)r^2}\right) + \frac{(R_e^2 - r^2)D}{r^2(R_e^2 - 1)} \\
&+ \frac{B}{2}\left(\frac{R_e^2(R_e^4 + R_e^2 + 4)}{(R_e^2 - 1)^3} + \frac{3R_e^4(R_e^2 + 1)}{(R_e^2 - 1)^3 r^4} - 4\frac{R_e^2(R_e^4 + R_e^2 + 1)}{(R_e^2 - 1)^3 r^2}\right)\cos 2\theta \\
&+ \frac{2\eta}{r^2}\left[\int_{1}^{r} r'\Delta p(r')dr' - \frac{r^2 - 1}{R_e^2 - 1}\int_{1}^{R_e} r'\Delta p(r')dr'\right] \\
\sigma_\theta &= \frac{A}{2}\left(\frac{R_e^2}{R_e^2 - 1} + \frac{R_e^2}{(R_e^2 - 1)r^2}\right) - \frac{(R_e^2 + r^2)D}{r^2(R_e^2 - 1)} \\
&- \frac{B}{2}\left(\frac{R_e^2(R_e^4 + R_e^2 + 4)}{(R_e^2 - 1)^3} + \frac{3R_e^4(R_e^2 + 1)}{(R_e^2 - 1)^3 r^4} - \frac{12R_e^2 r^2}{(R_e^2 - 1)^3}\right)\cos 2\theta \\
&+ 2\eta\Delta p(r) - \frac{2\eta}{r^2}\left[\int_{1}^{r} r'\Delta p(r')dr' + \frac{r^2 - 1}{R_e^2 - 1}\int_{1}^{R_e} r'\Delta p(r')dr'\right]
\end{aligned}
\tag{2}
$$

where $A = \sigma_H + \sigma_h/p_e$, where $(A > 2)$, $B = \sigma_H + \sigma_h/p_e$, $D = p_w/p_e$, where $(D < 1)$, and $\Delta p(r) = p(r) - 1$.

The dimensionless effective stress distributions are:

$$
\begin{aligned}
\sigma_r' &= \sigma_r - \alpha_B p(r) = \frac{A}{2}\left(\frac{r_e^2}{r_e^2 - 1} - \frac{r_e^2}{(r_e^2 - 1)r^2}\right) + \frac{(r_e^2 - r^2)D}{r^2(r_e^2 - 1)} \\
&+ \frac{B}{2}\left(\frac{r_e^2(r_e^4 + r_e^2 + 4)}{(r_e^2 - 1)^3} + \frac{3r_e^4(r_e^2 + 1)}{(r_e^2 - 1)^3 r^4} - 4\frac{r_e^2(r_e^4 + r_e^2 + 1)}{(r_e^2 - 1)^3 r^2}\right)\cos 2\theta \\
&+ \frac{2\eta}{r^2}\left[\int_{1}^{r} r'\Delta p(r')dr' - \frac{r^2 - 1}{r_e^2 - 1}\int_{1}^{r_e} r'\Delta p(r')dr'\right] - \alpha_B p(r) \\
\sigma_\theta' &= \sigma_\theta - \alpha_B p(r) = \frac{A}{2}\left(\frac{r_e^2}{r_e^2 - 1} + \frac{r_e^2}{(r_e^2 - 1)r^2}\right) - \frac{(r_e^2 + r^2)D}{r^2(r_e^2 - 1)} \\
&- \frac{B}{2}\left(\frac{r_e^2(r_e^4 + r_e^2 + 4)}{(r_e^2 - 1)^3} + \frac{3r_e^4(r_e^2 + 1)}{(r_e^2 - 1)^3 r^4} - \frac{12r_e^2 r^2}{(r_e^2 - 1)^3}\right)\cos 2\theta \\
&+ 2\eta\Delta p(r) - \frac{2\eta}{r^2}\left[\int_{1}^{r} r'\Delta p(r')dr' + \frac{r^2 - 1}{r_e^2 - 1}\int_{1}^{r_e} r'\Delta p(r')dr'\right] - \alpha_B p(r)
\end{aligned}
\tag{3}
$$

where α_B is the Biot parameter.

3 Analysis of the influence of acceleration effect on the wellbore stress

The traditional Darcy–Forchheimer model is not suitable for characterizing the flow of high-pressure gas into the well, so the acceleration effect of gas should be considered (Jin et al., 2011; Chen et al., 2011; Jin et al., 202). The acceleration effect of near-wellbore gas can be characterized by the dimensionless quantity λ. After considering the acceleration effect, the three characteristics of gas flow in high-pressure gas wells are:

1) With the decrease of bottomhole pressure, there is a maximum mass flow rate of fluid into the well, $m_{\max}$.

$$
m_{\max} = \sqrt{\lambda}D
\tag{4}
$$

2) The gas pressure gradient of the three flow models which are Darcy's law, the Darcy-Forchheime model and the Darcy-Forchheime model considering gas acceleration has the

FIGURE 1
The effective radial stress distribution for the three flow models.
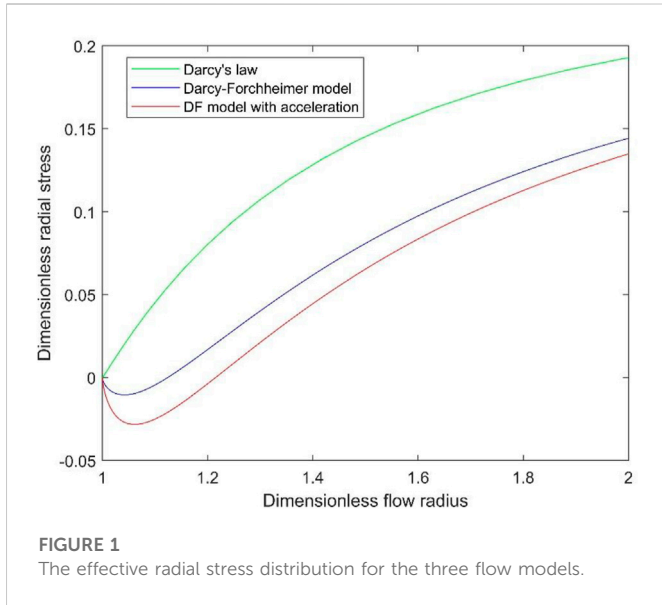
following relation when the mass flow is the same. The subscript *AC* stands for the Darcy-Forchheime model considering gas acceleration, *DF* is the Darcy-Forchheime model, and *D* points to Darcy's law.

$$\left(\frac{dp}{dr}\right)_{AC} > \left(\frac{dp}{dr}\right)_{DF} > \left(\frac{dp}{dr}\right)_{D} \tag{5}$$

3) Under the same mass flow rate, the bottomhole pressure of the three models has the following relationship.

$$(D)_{AC} < (D)_{DF} < (D)_{D} \tag{6}$$

3.1 Comparative analysis of effective radial stress

Jin et al. (2011b) believed that the effective radial stress in the near-wellbore zone is more likely to change into tensile stress after considering the acceleration effect, but he did not give the relative size for the effective radial stress of the three flow models. To facilitate the analysis of this relationship, the inhomogeneity of *in-situ* stress is ignored, i.e., *B*=0, and the Biot parameter is equal to 1. According to Eq. 3, $\sigma_r'|_{r=1,\alpha_B=1} = 0$ for the three flow models.

The derivative of effective radial stress for Darcy's law is:

$$\left(\frac{d\sigma_r'}{dr}\Big|_{r=1}\right)_D = \frac{d\sigma_r}{dr}\Big|_{r=1} - \frac{dp}{dr}\Big|_{r=1}$$

$$= \frac{r_e^2 A}{r_e^2 - 1} - 2\left(\frac{r_e^2}{r_e^2 - 1} - \eta\right)D_D - 2\eta \bar{p}_D - \frac{m_D}{D_D} \tag{7}$$

where $\bar{p}_D = 2/r_e^2 - 1 \int_1^{r_e} (r' p(r'))dr'$.

The derivative of effective radial stress for the Darcy–Forchheimer model can be given by

$$\left(\frac{d\sigma_r'}{dr}\Big|_{r=1}\right)_{DF} = \frac{d\sigma_r}{dr}\Big|_{r=1} - \frac{dp}{dr}\Big|_{r=1}$$

$$= \frac{r_e^2 A}{r_e^2 - 1} - 2\left(\frac{r_e^2}{r_e^2 - 1} - \eta\right)D_{DF} - 2\eta \bar{p}_{DF}$$

$$- \frac{1}{D_{DF}}\left(m_{DF} + \frac{\delta}{\lambda}m_{DF}^2\right) \tag{8}$$

where δ/λ is constant.

The derivative of effective radial stress for the Darcy–Forchheimer model considering gas acceleration becomes

$$\left(\frac{d\sigma_r'}{dr}\Big|_{r=1}\right)_{AC} = \frac{d\sigma_r}{dr}\Big|_{r=1} - \frac{dp}{dr}\Big|_{r=1}$$

$$= \frac{r_e^2 A}{r_e^2 - 1} - 2\left(\frac{r_e^2}{r_e^2 - 1} - \eta\right)D_{AC} - 2\eta \bar{p}_{AC}$$

$$- \frac{1}{D_{AC}}\frac{m_{AC} + \frac{\delta}{\lambda}m_{AC}^2 + m_{AC}^2/\lambda}{1 - \left(m_{AC}^2/(\lambda D_{AC}^2)\right)} \tag{9}$$

The difference in derivative of effective stress on the wellbore between Darcy's law and Darcy–Forchheimer model with the same mass flow rate is:

$$\left(\frac{d\sigma_r'}{dr}\Big|_{r=1}\right)_D - \left(\frac{d\sigma_r'}{dr}\Big|_{r=1}\right)_{DF} = m\left(\frac{1}{D_{DF}} - \frac{1}{D_D}\right) + \frac{\delta}{\lambda}\frac{m^2}{D_{DF}}$$

$$- \left[2\eta(\bar{p}_D - \bar{p}_{DF}) + 2\left(\frac{r_e^2}{r_e^2 - 1} - \eta\right)\right.$$

$$\left.(D_D - D_{DF})\right] \tag{10}$$

where, $2\eta(\bar{p}_D - \bar{p}_{DF}) + 2(r_e^2/r_e^2 - 1 - \eta)(D_D - D_{DF}) < 2(r_e^2/r_e^2 - 1 - \eta)$ $(D_D - D_{DF})$.

We can obtain $(d\sigma_r'/dr|_{r=1})_D - (d\sigma_r'/dr|_{r=1})_{DF} > 0$ labeled Equation 11, when $m \geq \frac{\frac{1}{D_D} - \frac{1}{D_{DF}} + \sqrt{\left(\frac{1}{D_{DF}} - \frac{1}{D_D}\right)^2 + 8\frac{\delta}{\lambda D_{DF}}\left(\frac{r_e^2}{r_e^2 - 1} - \eta\right)(D_D - D_{DF})}}{2\delta/\lambda/D_{DF}} = m_1$.

The given distance r_a must exist. $(\sigma_r')_D > (\sigma_r')_{DF}$, when the radius in polar coordinates is between 1 and r_a, i.e., $1 < r < r_a$, combining $\sigma_r'|_{r=1,\alpha_B=1} = 0$.

The difference in derivative of effective stress on the wellbore between Darcy–Forchheimer model and Darcy–Forchheimer model considering gas acceleration with the same mass flow rate is:

$$\left(\frac{d\sigma_r'}{dr}\Big|_{r=1}\right)_{DF} - \left(\frac{d\sigma_r'}{dr}\Big|_{r=1}\right)_{AC} = \frac{1}{D_{AC}}\frac{m + \frac{\delta}{\lambda}m^2 + m^2/\lambda}{1 - (m_{AC}^2/(\lambda D_{AC}^2))} - \frac{1}{D_{DF}}\left(m + \frac{\delta}{\lambda}m^2\right)$$

$$- \left[2\eta(\bar{p}_{DF} - \bar{p}_{AC}) + 2\left(\frac{r_e^2}{r_e^2 - 1} - \eta\right)(D_{DF} - D_{AC})\right]$$

where $\frac{1}{D_{AC}}\frac{m + \frac{\delta}{\lambda}m^2 + m^2/\lambda}{1 - (m_{AC}^2/(\lambda D_{AC}^2))} - \frac{1}{D_{DF}}(m + \frac{\delta}{\lambda}m^2) > \frac{m + \frac{\delta}{\lambda}m^2 + m^2/\lambda}{D_{AC}} - \frac{1}{D_{DF}}(m + \frac{\delta}{\lambda}m^2) > m^2[\frac{\delta}{\lambda}(\frac{1}{D_{AC}} - \frac{1}{D_{DF}}) + \frac{1}{\lambda D_{AC}}]$, and $2\eta(\bar{p}_{DF} - \bar{p}_{AC}) + 2(\frac{r_e^2}{r_e^2 - 1} - \eta)(D_{DF} - D_{AC}) < 2(\frac{r_e^2}{r_e^2 - 1} - \eta)(D_{DF} - D_{AC})$.

We can find $(\frac{d\sigma_r'}{dr}|_{r=1})_{DF} - (\frac{d\sigma_r'}{dr}|_{r=1})_{AC} > 0$, which is marked as Equation 12 when $m \geq \sqrt{\frac{2(r_e^2/r_e^2 - 1 - \eta)(D_{DF} - D_{AC})}{\frac{\delta}{\lambda}(1/D_{AC} - 1/D_{DC}) + 1/D_{\lambda AC}}} = m_2$.

As well, the given distance r_b must exist. $(\sigma_r')_{DF} > (\sigma_r')_{AC}$, when the radius in polar coordinates is between 1 and r_b, i.e., $1 < r < r_b$, combining $\sigma_r'|_{r=1,\alpha_B=1} = 0$.

Combining equation 11 and 12, we can get $(\sigma_r')_D > (\sigma_r')_{DF} > (\sigma_r')_{AC}$, when $\sqrt{\lambda}D_{AC} \geq m \geq \max(m_1, m_2)$ and $1 < r < \min(r_a, r_b)$.
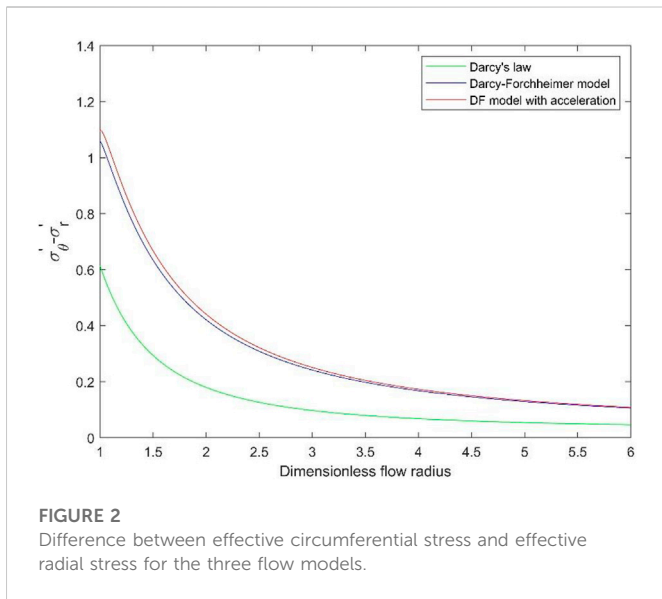
FIGURE 2
Difference between effective circumferential stress and effective
radial stress for the three flow models.
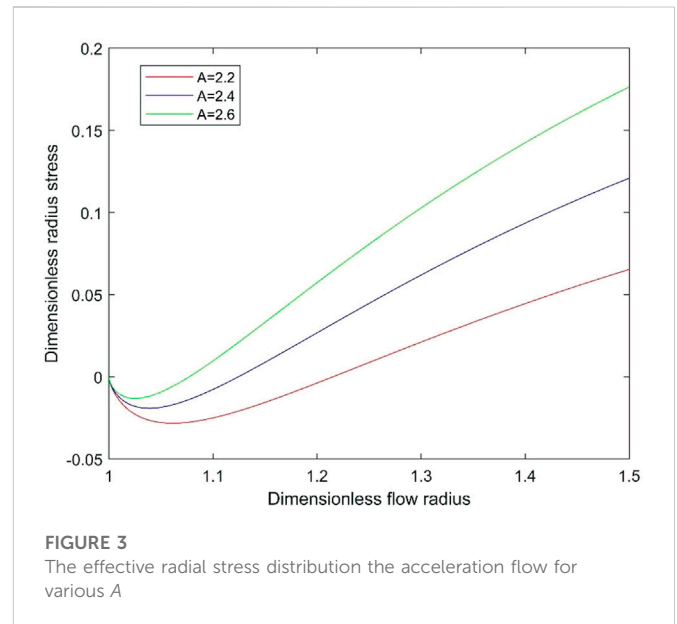
FIGURE 3
The effective radial stress distribution the acceleration flow for
various A

It is quite clear that $(\sigma_r')_D > (\sigma_r')_{DF} > (\sigma_r')_{AC}$ even if $\alpha_B < 1$.

Effective radial stress near the wellbore must be a negative value when $d(\sigma_r')_{AC}/dr|_{r=1} < 0$. We can find that the effective radial stress is minimal for the Darcy–Forchheimer model considering gas acceleration because $(\sigma_r')_D > (\sigma_r')_{DF} > (\sigma_r')_{AC}$. In other words, the tensile stress is minimal for the Darcy–Forchheimer model considering gas acceleration.

According to Equations 7 and 8 and 9, we can obtain $(d\sigma_r/dr)_D < (\sigma_r/dr)_{DF} < (\sigma_r/dr)_{AC}$ and the pore pressure gradient plays a decisive role in the effective radial stress by using Equation 5.

To better observe the variation in tensile stress, a case is presented. The mass flow rate, m, equals 0.0412 which is bigger than the maximum between m_1 equal to 0.0232 and m_2.given by 0.0245. Set other parameters as follows. $r_e = 2000$, $\eta = 0.5$, $\lambda = 0.5$, $\delta = 50$, $A = 2.2$, and $B = 0$. In the above parameters, the distribution of the stress for the three flow models is illustrated in Figure 1. Firstly, for Darcy's law, the effective radial stress on the wellbore is zero, which is the minimum in the stress distribution. Secondly, for the Darcy-Forchheimer model, the effective radial stress at r=1.0395 equals −0.0105, which is the minimum. Finally, for the Darcy-Forchheimer model, the effective radial stress is equal to −0.0282 at r=1.0568, which is the minimum, i.e., it is 2.82MPA when the formation pressure is 100 MPa.

3.2 Difference between effective circumferential stress and effective radial stress

For the convenience of comparative analysis, the inhomogeneity of *in-situ* stress is not considered here, and the Biot parameter is assumed to be one.

From Equation 2, we can conclude that

$$\sigma_\theta|_{r=1} = \frac{r_e{}^2 A - (r_e{}^2 + 1)D}{r_e{}^2 - 1} + 2\eta(D-1)$$

$$= \left(\frac{A}{1 - \frac{1}{r_e^2}} - 2\eta\right) - \left(\frac{1 + \frac{1}{r_e^2}}{1 - \frac{1}{r_e^2}} - 2\eta\right)D$$

where $\frac{A}{1 - \frac{1}{r_e^2}} - 2\eta > 0$, and $\frac{1 + \frac{1}{r_e^2}}{1 - \frac{1}{r_e^2}} - 2\eta > 0$.

When the mass flow rates of the three flow models are the same, the wellbore pressure can be written as $(D)_{AC} < (D)_{DF} < (D)_D$. Then, we have $(\sigma_\theta|_{r=1})_{AC} > (\sigma_\theta|_{r=1})_{DF} > (\sigma_\theta|_{r=1})_D$ and $(\sigma_\theta'|_{r=1})_{AC} > (\sigma_\theta'|_{r=1})_{DF} > (\sigma_\theta'|_{r=1})_D$.

Because the effective radial stresses on the wellbore for the three flow models are zero, it can be obtained that

$$\left(\sigma_\theta'|_{r=1} - \sigma_r'|_{r=1}\right)_{AC} > \left(\sigma_\theta'|_{r=1} - \sigma_r'|_{r=1}\right)_{DF} > \left(\sigma_\theta'|_{r=1} - \sigma_r'|_{r=1}\right)_D \quad (11)$$

It is quite clear that Equation 13 is correct, even if $\alpha_B < 1$. When $1 < r < r_e$, from Equation 3, we have

$$\sigma_\theta' = \frac{r_e^2(r^2+1)A}{2r^2(r_e^2-1)} - \frac{r_e^2+r^2}{r^2(r_e^2-1)}D + (2\eta - \alpha_B)p(r)$$
$$- \frac{2\eta}{r^2}\left[\int_1^r r'p(r')dr' + \frac{r^2-1}{r_e^2-1}\int_1^{r_e} r'p(r')dr'\right] - \frac{2\eta}{r^2}$$

As long as $\eta \le \alpha_B/2$, σ_θ' and $p(r)$ are negatively correlated for the same mass flow rate. Then we can conclude that $(\sigma_\theta')_{AC} > (\sigma_\theta')_{DF} > (\sigma_\theta')_D$, where $1 \le r < r_e$. The accelerating flow has the highest difference:

$$\left(\sigma_\theta' - \sigma_r'\right)_{AC} > \left(\sigma_\theta' - \sigma_r'\right)_{DF} > \left(\sigma_\theta' - \sigma_r'\right)_D \quad (12)$$

To better observe the variation in the difference between effective circumferential stress and effective radial stress, a case is presented. When the other parameters are set to $m = 0.0412$, $r_e = 2000$, $\eta = 0.5$, $\lambda = 0.5$, $\delta = 50$, $A = 2.2$, and $B = 0$, the difference is shown in Figure 2. The difference between effective circumferential stress and effective radial stress reaches the maximum at r=1, which is equal to 0.6147, for Darcy's law. It becomes 1.0004 reaching the maximum at r=1.0584 for Darcy–Forchheimer models. Meanwhile, For the acceleration flow, this difference equals 1.0980 at r=1.0063 which is the maximum in the distribution. When the formation pressure is 100MPa, the maximum for the three flow models is 61.47MPa, 100.04 MPa and 109.80 MPa respectively.

FIGURE 4
The effective radial stress distribution in the acceleration flow for various *B*

FIGURE 5
Difference between effective circumferential stress and effective radial stress in the acceleration flow for various A.

FIGURE 6
Difference between effective circumferential stress and effective radial stress in the acceleration flow for various B.
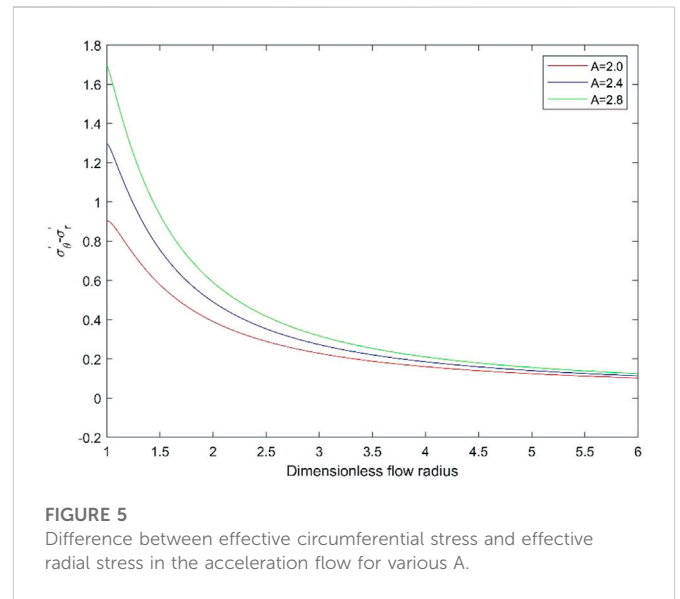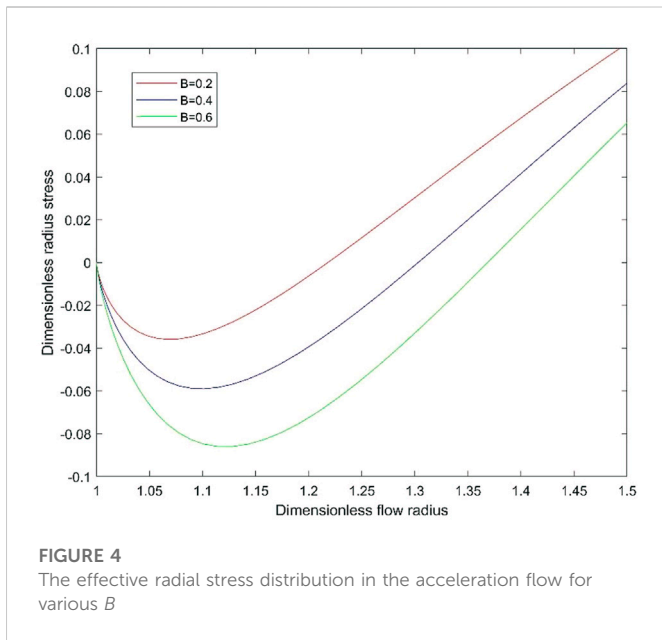
4 Analysis of the influence of *in situ* stress on the wellbore stress

4.1 Comparative analysis of effective radial stress

Since $r_e^2/r_e^2 - 1 - r_e^2/(r_e^2 - 1)r^2 > 0$, we have $\frac{d\sigma_r'}{dA} > 0$. Thus, the effective radial stress considering the acceleration effect is the monotone-increasing function of *A*. When the effective radial stress is negative, the smaller *A* is, the greater the tensile stress is, indicating that the formation fluid is under abnormally high pressure, while the tensile stress is greater.

We plot the effective radial stress for $m = 0.0412$, $r_e = 2000$, $\eta = 0.5$, $\lambda = 0.5$, $\delta = 50$ and $B = 0$ in Figure 3. It shows that the effective radial stress is the minimum at r=1.0568, which is −0.0282 when A=2.2. While A=2.4, the effective radial stress is −0.0191 at r=1.0395 which is also minimum. When A=2.6, the mini effective radial stress is −0.0132 at r=1.0253. When $1 < r < \sqrt{\frac{3+3/r_e^2}{1+1/r_e^2+4/r_e^4}}$ and $\cos 2\theta > 0$, we have $(\frac{r_e^2(r_e^4+r_e^2+4)}{(r_e^2-1)^3} + \frac{3r_e^4(r_e^2+1)}{(r_e^2-1)^3 r^4} - \frac{12r_e^2 r^2}{(r_e^2-1)^3}) \cos 2\theta < 0$.

Thus, $d\sigma_r'/dB < 0$. It can be seen that the effective radial stress considering the acceleration effect is a monotone-decreasing function of *B*. When the effective radial stress is tensile, the stronger the non-uniformity of *in-situ* stress is, the smaller the effective radial stress is, that is, the greater the tensile stress is and the maximum tensile stress is obtained in the direction of the maximum horizontal principal stress.

In Figure 4, we plot the effective circumferential stress for $m = 0.0412$, $r_e = 2000$, $\eta = 0.5$, $\lambda = 0.5$, $\delta = 50$, $A = 2.4$ and $\theta = 0$. In the direction of the maximum horizontal principal stress, the minimum effective radial stress is −0.0359 at r=1.0667 when B=0.2. When B=0.4, the effective radial stress is the minimum at r=1.1010, which is −0.0590. When B=0.6, it is the minimum at r=1.1278, which is −0.0859.
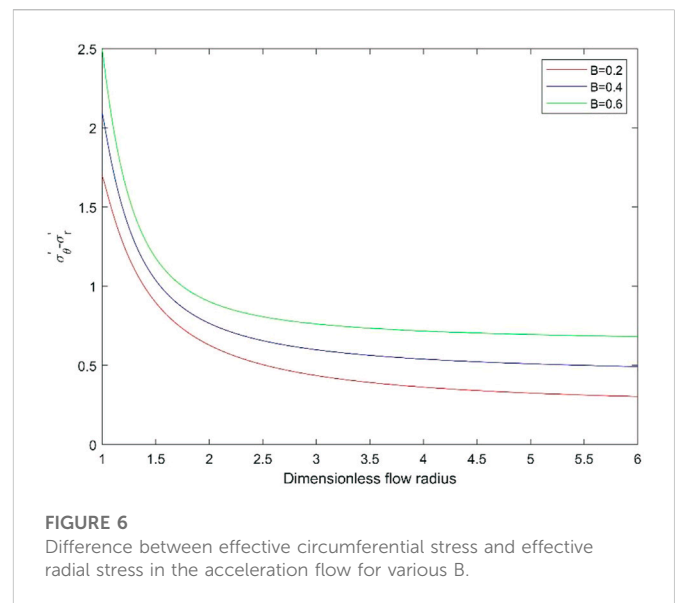
4.2 Difference between effective circumferential stress and effective radial stress

From Equation 3, the difference between effective circumferential stress and effective radial stress in the acceleration flow is given by

$$\sigma_\theta' - \sigma_r' = \frac{Ar_e^2}{(r_e^2 - 1)r^2} - \frac{2D}{(r_e^2 - 1)} + 2\eta\Delta p(r) - \frac{4\eta}{r^2}\int_1^r r'\Delta p(r')dr'$$
$$- B\cos 2\theta \left[\frac{r_e^2(r_e^4 + r_e^2 + 4)}{(r_e^2 - 1)^3} + \frac{3r_e^4(r_e^2 + 1)}{(r_e^2 - 1)^3 r^4} - \frac{6r_e^2 r^2}{(r_e^2 - 1)^3}\right.$$
$$\left. + 2\frac{r_e^2(r_e^4 + r_e^2 + 1)}{(r_e^2 - 1)^3 r^2}\right] \tag{13}$$

It is obvious that $d(\sigma_\theta' - \sigma_r')/dA > 0$, so the value, $\sigma_\theta' - \sigma_r'$, is smaller when the formation pressure is from the normal pressure to the abnormally high pressure.

The parameters in Figure 5 are the same as that in Figure 3. When A=2.0, the maximum stress is 0.9014 at r=1.0142. When A=2.4, when r= 1.0036, the value, $\sigma_\theta' - \sigma_r'$, is 1.2963. When A=2.8, $\sigma_\theta' - \sigma_r'$ reaches its maximum value at r=1.004, which is 1.6950.

It can be written as $F(r) = \frac{r_e^2(r_e^4 + r_e^2 + 4)}{(r_e^2 - 1)^3} + \frac{3r_e^4(r_e^2 + 1)}{(r_e^2 - 1)^3 r^4} - \frac{6r_e^2 r^2}{(r_e^2 - 1)^3} + 2\frac{r_e^2(r_e^4 + r_e^2 + 1)}{(r_e^2 - 1)^3 r^2}$.

When $1 \le r \le r_e$, $\frac{dF(r)}{dr} < 0$ and $F(r) \ge \frac{r_e^6 - 3r_e^4 + 9r_e^2 + 5}{(r_e^2 - 1)^3} > 0$. Thus, $\frac{d(\sigma_\theta' - \sigma_r')}{dB} > 0$, for $\cos 2\theta < 0$. These imply that the greater the stress non-uniform, the greater the value $\sigma_\theta' - \sigma_r'$.

In Figure 6, we plot the difference between effective circumferential stress and effective radial stress in the acceleration flow for $m = 0.0412$, $r_e = 2000$, $\eta = 0.5$, $\lambda = 0.5$, $\delta = 50$, $A = 2.4$ and $\theta = \pi/2$. When B=0.2, the maximum stress is 1.6947 at r=1.0004. When B=0.4, when r=1.0004, the value, $\sigma_\theta' - \sigma_r'$, is 2.0940. When B=0.6, $\sigma_\theta' - \sigma_r'$ reaches its maximum value at r=1, which is 2.4938.

5 Wellbore stability of uncased hole in the high-pressure gas wells

5.1 Tensile fracture

According to the analysis in section 3.1 of this paper, when the stress of the surrounding rock near the wellbore reaches the tensile strength, the acceleration flow requires less mass flow than the Darcy model and the Darcy-Forhheimer model, that is, the surrounding rock near the wellbore is the first to fail in the s acceleration flow. According to the analysis in section 4.1 of this paper, tensile failure occurs first in the surrounding rock near the wellbore in the direction of maximum horizontal principal stress.

We will assume the Biot parameter $\alpha_B = 1$, so $\sigma_r'|_{r=1,\alpha_B=1} = 0$. Thus, the effective tensile stress depends on the positive or negative sign of the effective radial stress derivative at the wellbore. In other words, the condition for the onset of effective tensile stress is $d\sigma_r'/dr|_{r=1} = 0$. Combining the condition, Equation 9 can be written as

$$\frac{-r_e^{2*}(A - 2D - Ar_e^2 + 2Dr_e^2 + 4B\cos 2\theta + 2Br_e^2\cos 2\theta)}{(r_e^2 - 1)^2} - 2D$$
$$-\frac{2D}{r_e^2 - 1} - 2\eta(\bar{p} - D) - \frac{1 - D^2}{2D\ln r_e} = 0$$

The critical bottomhole pressure, D, for the onset of tensile stress is determined from the above equation.

5.2 Shear failure

It is assumed that the shear failure of rock follows the weak surface failure criterion (Zeng et al., 2021). The Mohr-Coulomb failure criterion for $\beta < \beta_1$ or $\beta > \beta_2$ is defined as

$$\sigma_1 - \sigma_3 = \frac{2(C_w + \tan\phi_w \sigma_3)}{(1 - \tan\phi_w \cot\beta)\sin 2\beta}$$

$$\beta_1 = \frac{\phi_w}{2} + \frac{1}{2}\arcsin\left[\frac{(\sigma_1 + \sigma_3 + 2C_w \cot\phi_w)\sin\phi_w}{\sigma_1 - \sigma_3}\right]$$

$$\beta_2 = \frac{\pi}{2} + \frac{\phi_w}{2} - \frac{1}{2}\arcsin\left[\frac{(\sigma_1 + \sigma_3 + 2C_w \cot\phi_w)\sin\phi_w}{\sigma_1 - \sigma_3}\right]$$

where C_o is the cohesion of the rock, ϕ_o is the friction angle of the rock, C_w is the cohesion of the weak plane, ϕ_w is the friction angle of the weak plane, and β is the angle between maximum principal stress and weak plane normal, related to the failure mode of the anisotropic mudstone with the weak plane.

Only the case is discussed where $\sigma_\theta' > \sigma_z' > \sigma_r'$ and weak plane shear failure occurred in the rock. According to the analysis in section 3.2, shear failure occurs first in the surrounding rock of the acceleration flow when the mass flow rate increases and shear failure occurs first in the minimum horizontal direction of the surrounding rock according to the analysis in section 4.2.

Thus, when r=1, Equation 13 can be written as

$$\left(\sigma_\theta' - \sigma_r'\right)_{r=1} = A\frac{r_e^2}{r_e^2 - 1} - \frac{B}{2}\frac{4r_e^2(r_e^2 + 2)}{(r_e^2 - 1)^2}\cos 2\theta$$
$$-D\frac{r_e^2 + 2}{r_e^2 - 1} - (1 - 2\eta)D - 2\eta \tag{14}$$

Thus, $D = \frac{\sin 2\beta(1 - \mu_w \cot\beta)\left(A\frac{r_e^2}{r_e^2 - 1} - 2B\frac{r_e^2(r_e^2 + 2)}{(r_e^2 - 1)^2}\cos 2\theta - 2\eta\right) + 2C_w}{\frac{r_e^2 + 2}{r_e^2 - 1} + (1 - 2\eta) + 2\mu_w(1 - \alpha_B)}$.

The critical bottomhole pressure is proportional to the Biot parameter, that is, when the Biot parameter increases, the mass flow required for shear failure decreases. When the Biot parameter increases, the effective radial stress decreases, the tensile stress increases and the required pore pressure gradient decreases. In other words, when the Biot parameter increases, the mass flow rate required for tensile failure decreases. Therefore, the Biot parameter has the same effect on tensile failure and shear failure.

6 Conclusion

Considering the dual effects of non-uniformity of *in-situ* stress and acceleration effect in the process of seepage, the stress state of surrounding rock suitable for high-pressure gas well and its influence on tensile failure and shear failure in the process of gas test of the high-pressure gas well are analyzed, and the following conclusions are as following.

1) Considering the acceleration effect, the difference between effective circumferential stress and effective radial stress at any flow radius is larger than that in the other two flow models, which is more likely to cause shear failure. The difference between the effective circumferential stress and the effective radial stress does not reach the maximum value at the wellbore wall.
2) The pore pressure gradient plays a decisive role in the effective radial stress. Considering the acceleration effect, the minimum effective radial stress is smaller than that of the other two flow models, which is more likely to lead to tensile failure. The conditional expression of tensile stress generation considering the non-uniformity of *in-situ* stress is given.
3) The influence of Biot parameter on tensile failure and shear failure is the same.

Data availability statement

The original contributions presented in the study are included in the article/supplementary material, further inquiries can be directed to the corresponding author.

Author contributions

HJ and MC contributed to conception and design of the study. CH organized the database. XL performed the statistical analysis. YZ wrote the first draft of the manuscript. All authors contributed to manuscript revision, read, and approved the submitted version.

Funding

Conflict of interest

Author CH was employed by the company Xi'an Qing'an Electrical Control Co., Ltd., China.

The remaining authors declare that the research was conducted in the absence of any commercial or financial relationships that could be construed as a potential conflict of interest.

Publisher's note

All claims expressed in this article are solely those of the authors and do not necessarily represent those of their affiliated organizations, or those of the publisher, the editors and the reviewers. Any product that may be evaluated in this article, or claim that may be made by its manufacturer, is not guaranteed or endorsed by the publisher.

References

Chang, Z., and Hou, B. (2022). Numerical simulation on cracked shale oil reservoirs multi-cluster fracturing under inter-well and inter-cluster stress interferences. *Rock Mech. Rock Eng.* In Press. doi:10.1007/s00603-022-03145-7

Chen, K. P. (2011). A new mechanistic model for prediction of instantaneous coal outbursts—dedicated to the memory of prof. Daniel D. Joseph. *Int. J. Coal Geol.* 87 (2), 72–79. doi:10.1016/j.coal.2011.04.012

Fjaer, E., Holt, R. M., Horsrud, P., Raaen, A. M., and Risnes, R. (2008). *Petroleum related rock mechanics.* 2nd ed. Amsterdam: Elsevier.

Hou, B., Chang, Z., and Wu, A. (2022b). Simulation of competitive propagation of multi-fractures on shale oil reservoir multi-clustered fracturing in Jimsar sag. *Acta Pet. Sin.* 43 (01), 75–90. doi:10.7623/xyxb202201007

Hou, B., Cui, Z., Ding, J. H., Zhang, F. S., Zhuang, L., and Elsworth, D. (2022a). Perforation optimization of layer-penetration fracturing for commingling gas production in coal measure strata. *Petroleum Sci.* 19 (4), 1718–1734. doi:10.1016/j.petsci.2022.03.014

Hou, B., and Cui, Z. (2022e). Vertical fracture propagation behavior upon supercritical carbon dioxide fracturing of multiple layers. *Eng. Fract. Mech.*, 108913. In Press. doi:10.1016/j.engfracmech.2022.108913

Hou, B., Dai, Y., Fan, M., Zhang, K., Wick, T., and Lee, S. (2022c). Numerical simulation of pores connection by acid fracturing based on phase field method. *Acta Pet. Sin.* 43 (6), 849–859. doi:10.7623/syxb202206009

Hou, B., Zhang, Q., Liu, X., Pang, H., and Zeng, Y. (2022d). Integration analysis of 3D fractures network reconstruction and frac hits response in shale wells. *Energy* 260, 124906. doi:10.1016/j.energy.2022.124906

Huang, L., He, R., Yang, Z., Tan, P., Chen, W., Li, X., et al. (2022). Exploring hydraulic fracture behavior in glutenite formation with strong heterogeneity and variable lithology based on DEM simulation. *Eng. Fract. Mech.* 278, 109020. doi:10.1016/j.engfracmech.2022.109020

Jiang, H., Chen, M., Jin, Y., and Chen, K. P. (2015a). Analytical modeling of acceleration-induced conductivity damage in a propped hydraulic fracture of a high-pressure gas well. *J. Nat. Gas Sci. Eng.* 26, 185–192. doi:10.1016/j.jngse.2015.06.019

Jiang, H., Chen, M., Jin, Y., and Chen, K. P. (2015c). Gas expansion-induced acceleration effect of a highly compressible gas flow in porous media. *J. Porous Media* 18 (8), 825–834. doi:10.1615/jpormedia.v18.i8.70

Jiang, H., Chen, M., Jin, Y., and Chen, K. P. (2015b). Importance of gas acceleration near the wellbore in radial compressible porous media flows for a vertical gas well. *Transp. Porous Media* 110 (1), 127–140. doi:10.1007/s11242-015-0559-9

Jiang, H., Dou, Y., Xi, Z., Chen, M., and Jin, Y. (2016). Microscopic choked flow for a highly compressible gas in porous media. *J. Nat. Gas Sci. Eng.* 35, 42–53. doi:10.1016/j.jngse.2016.08.039

Jin, Y., Chen, K. P., and Chen, M. (2011b). Development of tensile stress near a wellbore in radial porous media flows of a high pressure gas. *Int. J. Rock Mech. Min. Sci.* 48 (8), 1313–1319. doi:10.1016/j.ijrmms.2011.09.013

Jin, Y., Chen, K. P., Chen, M., and Grapsas, N. (2012). Gas expansion-induced acceleration effect in high-pressure gas flows near a wellbore. *J. porous media* 15 (4), 317–328. doi:10.1615/jpormedia.v15.i4.20

Jin, Y., Chen, K. P., Chen, M., Grapsas, N., and Zhang, F. X. (2011a). Short-time pressure response during the start-up of a constant-rate production of a high pressure gas well. *Phys. Fluids* 23 (4), 043101. doi:10.1063/1.3571494

Jin, Y., and Chen, K. P. (2019). Fundamental equations for primary fluid recovery from porous media. *J. Fluid Mech.* 860, 300–317. doi:10.1017/jfm.2018.874

Levy, A., Sorek, S., Ben-Dor, G., and Bear, J. (1995). Evolution of the balance equations in saturated thermoelastic porous media following abrupt simultaneous changes in pressure and temperature. *Transp. Porous Media* 21 (3), 241–268. doi:10.1007/BF00617408

Nield, D. A. (1994). Modelling high speed flow of a compressible fluid in a saturated porous medium. *Transp. porous media* 14 (1), 85–88. doi:10.1007/BF00617029

Sun, S., Wang, J., Le, H., Fan, H., and Wang, W. (2022). Experimental and numerical investigation on compressive strength and crack behavior of rock-like specimens with open flaws under confining loads. *Front. Earth Sci.* 10. doi:10.3389/feart.2022.972194

Tan, P., Jin, Y., and Pang, H. (2021). Hydraulic fracture vertical propagation behavior in transversely isotropic layered shale formation with transition zone using XFEM-based CZM method. *Eng. Fract. Mech.* 248, 107707. doi:10.1016/j.engfracmech.2021.107707

Warsitzka, M., Kukowski, N., and May, F. (2022). Patterns and failure modes of fractures resulting from forced folding of cohesive caprocks–comparison of 2D vs. 3D and single-vs. Multi-layered analog experiments. *Front. Earth Sci.* 10. doi:10.3389/feart.2022.881134

Wooding, R. (1957). Steady state free thermal convection of liquid in a saturated permeable medium. *J. Fluid Mech.* 2 (3), 273–285. doi:10.1017/S0022112057000129

Zeng, Y., Jiang, H., Ding, S., Chen, J., Wang, Y., and Zheng, J. (2021). Analytical and experimental investigations on mechanical properties of weak plane bedding in mudstone. *Geofluids* 2021, 5408701–5408705. doi:10.1155/2021/5408701

Zhang, Q., Hou, B., Lin, B., Liu, X., and Gao, Y. (2021). Integration of discrete fracture reconstruction and dual porosity/dual permeability models for gas production analysis in a deformable fractured shale reservoir. *J. Nat. Gas Sci. Eng.* 93, 104028. doi:10.1016/j.jngse.2021.104028

Zhang, W., Xue, X., Zhang, C., Qu, Y., Ke, K., Pan, S., et al. (2022). A drilling wellbore pressure calculation model considering the effect of gas dissolution and suspension. *Front. Earth Sci.* 10. doi:10.3389/feart.2022.993876

Zhao, X., Huang, B., and Grasselli, G. (2021). Numerical investigation of the fracturing effect induced by disturbing stress of hydrofracturing. *Front. Earth Sci.* 9. doi:10.3389/feart.2021.751626